ACS OMEGA

Open Access

http://pubs.acs.org/journal/acsodf

Article

PEG–PVP-Assisted Hydrothermal Synthesis and Electrochemical Performance of N-Doped MoS_2/C Composites as Anode Material for Lithium-Ion Batteries

Wei Liu,* Shenshen Yang, Dongsheng Fan, Yang Wu, Jingbo Zhang, Yaozong Lu, and Linping Fu

Cite This: *ACS Omega* 2024, 9, 9792–9802

Read Online

ACCESS | Metrics & More | Article Recommendations

ABSTRACT: Molybdenum disulfide shows promise as an anode material for lithium-ion batteries. However, its commercial potential has been constrained due to the poor conductivity and significant volume expansion during the charge/discharge cycles. To address these issues, in this study, N-doped MoS_2/C composites (NMC) were prepared via an enhanced hydrothermal method, using ammonium molybdate and thiourea as molybdenum and sulfur sources, respectively. Polyethylene glycol 400 (PEG400) and polyvinylpyrrolidone (PVP) were added in the hydrothermal procedure as soft template surfactants and nitrogen/carbon sources. The crystal structure, morphology, elemental composition, and surface valence state of the N-doped MoS_2/C composites were characterized by X-ray diffraction (XRD), field emission scanning electron microscopy (FESEM), high-resolution transmission electron microscopy (HRTEM), and X-ray photoelectron spectroscopy (XPS), respectively. The results indicate that the NMC prepared by this method are spherical particles with a nanoflower-like structure composed of MoS_2 flakes, having an average particle size of about 500 nm. XPS analysis shows the existence of C and N elements in the samples as C–N, C–C, and pyrrolic N. As anodes for LIBs, the NMC without annealing deliver an initial discharge capacity of 548.2 mAh·g^{-1} at a current density of 500 mA·g^{-1}. However, this capacity decays in the following cycles with a discharge capacity of 66.4 mAh·g^{-1} and a capacity retention rate of only 12% after 50 cycles. In contrast, the electrochemical properties of the counterparts are enhanced after annealing, which exhibits an initial discharge capacity of 575.9 mAh·g^{-1} and an ultimate discharge capacity of 669.2 mAh·g^{-1} after 70 cycles. The capacity retention rate decreases initially but later increases and elevated afterward to reach 116% at the 70th cycle, indicating an improvement in charge–discharge performance. The specimens after annealing have a smaller impedance, which indicates better charge transport and lithium-ion diffusion performance.

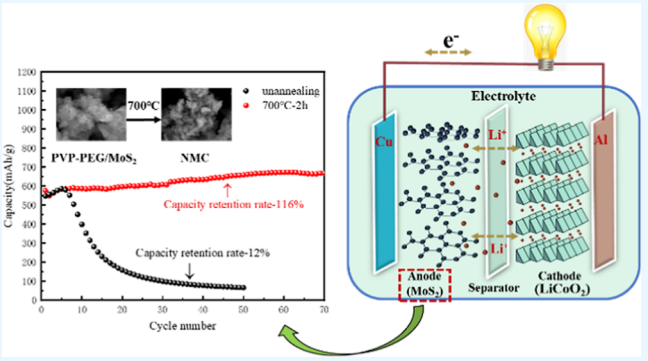

1. INTRODUCTION

With the rapid development of the global economy and population growth, the consumption rate of energy worldwide has greatly increased. The problem of energy exhaustion has become one of the major challenges faced by human society today as fossil energy is limited in stock and nonrenewable.[1−3] Additionally,[2] the combustion of fossil fuels will release a large number of harmful gases, which will cause serious harm to the ecology, such as the greenhouse effect. Therefore, the efficient conversion and full utilization of clean renewable energy have become a research hotspot. In recent years, the generation of renewable energy such as wind and solar energy has made great progress but is limited by the instability of its power source. Therefore, large-scale electrochemical energy storage devices with high capacity are crucial for the efficient utilization of clean energy.[4−7] In addition, the rapid development of portable electronic devices has also put forward higher requirements for the performance of the secondary battery. Lithium-ion batteries (LIBs) have attracted much attention and good application prospects in the field of energy storage due to their advantages such as relatively high volumetric energy density, rapid charge/discharge capacity, long cycle life, and better safety performance.[8−10] As an important component of LIBs, the anode material materials have become the key point to improve the electrochemical performances of LIBs.

Since the commercialization of LIBs, graphite has consistently been the predominant selection for an anode material. Although it exhibits many advantages such as good safety and

Received: December 15, 2023
Revised: January 31, 2024
Accepted: February 6, 2024
Published: February 16, 2024

low price, its theoretical specific capacity is too low (~372 $mAh{\cdot}g^{-1}$).[11] High-power LIBs are currently limited by the cathode material that can meet the capacity demand, but with the breakthrough of cathode material, it is of significant necessity to exploit and research a new-type anode material with high specific capacity.

As an alternative to the graphite anode, the molybdenum disulfide with a layered graphite-like structure has been extensively investigated because of its high theoretical specific capacity (~670 $mAh{\cdot}g^{-1}$),[12,13] low price, and abundant reservation. Nevertheless, there are some obstacles to its commercial applications,[14−17] such as structural collapse resulting from volume expansion during charge/discharge processes and relatively poor conductivity as a type of semiconductor material.

Thus, the primary objective of research aimed at improving the capacity of LIBs is to implement diverse strategies to enhance the charge−discharge performance, cycle stability, and conductivity of MoS_2-based anode materials.

Modulating the composition is an effective approach to increasing the conductivity of the material and achieving a higher capacity. Doping the nonmetallic N element effectively enhances the conductivity of MoS_2, ensuring optimal electron transport. Additionally, it accelerates the oxidation-related multielectron transport process by promoting the relatively high valence state of the Mo element. According to the literature review, nitrogen is a favorable element for stable doping into MoS_2 to increase its theoretical specific capacity by activating extra active sites and enhancing electrical conductivity.[18−20] Nanoflower-like N-doped MoS_2 was synthesized by Li et al.[21] via a simple, one-step hydrothermal method and used as anode materials for lithium-ion batteries. The N-doped MoS_2 anode material exhibits a specific capacity of 786 $mAh{\cdot}g^{-1}$ after 100 cycles at a high current density of 0.5C, indicating excellent cyclic stability compared to the pristine MoS_2. This excellent cycling performance is attributed to the superior electronic conductivity of N-doped MoS_2 anode materials, which provides a pathway for charge transport. Moreover, previous studies[22−25] indicated that the incorporation of carbon-based materials with molybdenum disulfide can greatly improve the conductivity of materials due to the high conductivity and specific surface area of the former. Carbon-based materials, such as graphene, carbon nanotubes (CNTs), and porous carbon, are commonly combined with molybdenum disulfide.

Therefore, it is hypothesized that the N element doping of the MoS_2 material combined with carbon would result in a positive effect on the electrochemical performance. It has been found that the N-doped porous carbon layer in N-MoS_2/C has both relatively high electrical conductivity and the ability to effectively retard the strain caused by the volume changes in the charge/discharge process. This layer also inhibits the accumulation or reaccumulation of MoS_2 during the lithium storage process. Yan-Hong Shi et al.[26] successfully integrate nanostructured MoS_2 into N-doped porous carbon through a simple one-step hydrothermal reaction. MoS_2/N−C microparticles greatly enhanced the electrical conductivity and electrochemical activity. Furthermore, the integration of nanoscale MoS_2 particles into porous carbon yields a unique structural benefit that effectively combines the advantages of nanoscale MoS_2 and micron-scale N-doped C. The particles exhibit excellent electrochemical behavior due to their increased surface area and improved conductivity. Consequently, the N-doped porous carbon materials serve as promising electrode materials for energy storage devices.

In addition to composition modulation, morphology regulation is also a crucial method for material synthesis and modification. Polyethylpyrrolidine (PVP) intercalated molybdenum disulfide (PVP/MoS_2) nanosheets with good interconnections were successfully prepared through an effective and versatile one-step hydrothermal strategy by Gu et al.[27] The structural characterization indicates that the incorporation of PVP molecules into MoS_2 leads to an enlarged interlayer spacing. The as-prepared PVP/MoS_2 nanomaterials exhibit exceptional absorption properties, due to the enhanced specific surface area and functional groups of PVP/MoS_2. Liu et al.[28] produced molybdenum disulfide nanosheets with severe lattice distortion through solvothermal methods, employing PEG400 as both a surfactant and a reactant. The incorporation of oxygen-containing and carbon-containing groups into the molybdenum disulfide interlayer leads to heterogeneous coupling of Mo−O−C and Mo−O, which modifies the microstructure of molybdenum disulfide and expands its layer spacing to 0.97 nm, significantly larger than the 0.615 nm of pristine MoS_2. This structure improves the electron transport rate and enhances the structural stability, allowing molybdenum disulfide to exhibit remarkable electrochemical properties without relying on carbon support or coating. As an anode material, it retains a capacity of 600 $mAh{\cdot}g^{-1}$ even after 1000 cycles at a current density of 0.5 $A{\cdot}g^{-1}$. Even at a high current density of 10 $A{\cdot}g^{-1}$, it maintains a capacity of 364 $mAh{\cdot}g^{-1}$, indicating an outstanding electrochemical performance.

Herein, nonmetallic nitrogen elements and composite carbon-based materials were doped to the MoS_2 matrix, to increase the number of charge carriers and inherent conductivity. Furthermore, surfactants were introduced to improve the structural stability by increasing the lattice spacing. The incorporation of these components will address the issues of high volume change rate, low conductivity, and suboptimal cycling performance found in pristine molybdenum disulfide when it is used as an anode material during the charging and discharging process. In this study, N-doped MoS_2/C composites (NMC) were synthesized by an enhanced hydrothermal process, using ammonium molybdate and thiourea as sources of molybdenum and sulfur, respectively, and surfactants PEG400 and PVP to assist the process. The crystal structure, morphology, elemental composition, valence distribution, and electrochemical properties of the as-prepared composites were characterized by X-ray diffraction (XRD), field emission scanning electron microscopy (FESEM), high-resolution transmission electron microscopy (HRTEM) and X-ray photoelectron spectroscopy (XPS), respectively. The effects of subsequent annealing on the properties of the powder were also investigated.

2. EXPERIMENTAL SECTION

2.1. Synthesis of N-MoS_2/C Composite. All chemical reagents used in the experiment were of analytical grade and used without further purification. In a typical synthesis process, 30 mL of polyethylene glycol 400 (PEG400, Tianjin Kermel Chemical Reagent Co., Ltd.) was first dissolved in 50 mL of deionized water, then 1.00 g sodium molybdate ($Na_2MoO_4{\cdot}2H_2O$, Tianjin Hengxin Chemical Co., Ltd.) and 1.84 g thiourea ($CS(NH_2)_2$, Tianjin Damao Chemical Reagent Co., Ltd.) were added in sequence during stirring. After being

https://doi.org/10.1021/acsomega.3c10031
ACS Omega 2024, 9, 9792−9802

completely dissolved, 0.15 g of polyvinylpyrrolidone (PVP, Rhawn reagent Co., Ltd.) was added and stirred for 60 min to obtain a clear starting solution. Then, it was transferred to a magnetic stirring autoclave lined with polytetrafluoroethylene (PTFE) and reacted at 220 °C for 8h. After cooling to room temperature, the residue was centrifuged and washed with ethanol and deionized water alternately four times and then dried at 60 °C for 12 h. Subsequently, the obtained N-MoS_2/C composite powder was annealed in a tubular furnace with argon (purity >99.999%) protection at 500 °C, 700, and 900 °C for 2 h at a heating rate of 5 °C/min and a flow rate of 250 mL/min. For comparison, MoS_2 was synthesized under identical experimental conditions without any surfactants or with only one single type of PEG400 and PVP.

2.2. Characterization of N-MoS_2/C Composite. The phase analysis of the sample was carried out using a D8-Advanced X-ray diffractometer (XRD, Bruker, Germany). The morphology and microstructure were characterized by a JSM-IT800SHL field emission scanning electron microscope (FESEM, Nippon Electronics, Japan) and a JEM-2100 High-resolution transmission electron microscope (HRTEM, Nippon Electronics, Japan). ESCALAB 250Xi K-Alpha + X-ray photoelectron spectrometer (XPS, Thermo Fischer Scientific, USA) was used to analyze the elemental composition and valence states of the samples.

2.3. Electrochemical Measurements. The capacities and cycling properties of the as-prepared samples were performed by CR2032 buckle cells assembled in an argon-filled glovebox (Mikrouna (Shanghai) Ind. Int. Tech. Co., Ltd.), with a lithium sheet as the counter electrode. The cyclic voltammetry (CV) and electrochemical impedance spectroscopy (EIS) tests were carried out at the CHI660E Electrochemical Workstation (CH Instruments, USA). The charge−discharge cycle performance and rate performance were tested on a CT2001A (Wuhan Land Electronics Co., Ltd., China) button battery test system.

3. RESULTS AND DISCUSSION

3.1. Crystal Structure, Morphology, and Composition. To investigate the effect of different types of surfactants on the microscopic morphology of MoS_2. MoS_2 materials were added with 0.15 g of PVP and 30 mLPEG400, and both surfactants were prepared, respectively. A control experiment was performed with MoS_2 without any added surfactant. As depicted in Figure 1, the FESEM images disclose the morphology of the obtained samples. The representative FESEM images of as-prepared samples are displayed in Figure 4a−d, revealing a porous nanosphere structure assembled from ultrathin MoS_2 nanosheets. Such an open porous structure is in favor of electronic contact and rapid electron transfer during the discharge/charge process. Figure 1a shows MoS_2 synthesized without any surfactant, which is composed of irregular spherical nanosheets. However, the average particle size is approximately 10 μm due to agglomeration. When PEG400 was added as the sole surfactant, it can be observed that the irregular surface of molybdenum disulfide transformed into small spheres, as shown in Figure 1b. The synthesized molybdenum disulfide yielded a microsphere with an average diameter of about 2−3 μm. Nevertheless, its dispersibility remained inadequate, as it clustered together to create large and irregularly shaped particles. When PVP was solely added, its refinement effect on the particle size was more prominent. Compared with the samples using PEG400, the MoS_2 synthesized with PVP has a smaller spherical structure with an average particle size of 900 nm, as displayed in Figure 1c.

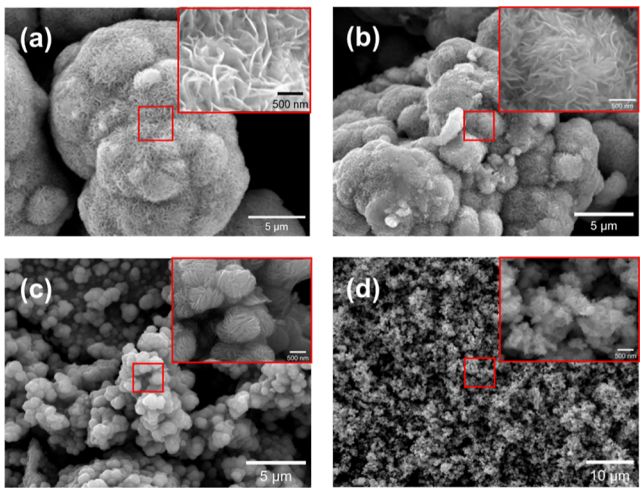

Figure 1. FESEM images of MoS_2 and NMC synthesized using different surfactants (a, no surfactant; b, PEG400; c, PVP; d, PEG400+PVP).

Additionally, the morphology images of MoS_2 synthesized from both PEG400 and PVP are presented in Figure 1d. It can be observed from the figures that the particles are further refined with good dispersion and uniformity evident at low multiples. While at high multiples, the material maintains a nanoflower-like structure with an average particle size of around 500 nm. PEG400 is dispersed into the solution to form a spatial steric site resistance effect. The mutual contact between the molybdenum disulfide nuclei was prevented, which led to the morphology of MoS_2 being transformed into microspheres. Therefore, the addition of PEG400 can refine the grain, but the dispersion is poor. When PVP was added to the molybdenum disulfide reaction system, it spontaneously assembled into a vesicular micelle with amide groups inside the outer alkyl backbone. It encapsulates the molybdenum disulfide nucleation core in solution to form a circular "microreactor". Molybdenum disulfide nanosheets are oriented to grow in a specific region of the "microreactor" and the size of the material is controlled. Therefore, the addition of PVP both alleviated the agglomeration of molybdenum disulfide and improved the dispersion. When both surfactants were added at the same time, MoS_2 showed uniformly dispersed fine particles.

Figure 2 displays the XRD patterns of the NMC specimens synthesized with varying surfactants. As the sample with no surfactant, four diffraction peaks located at 14.1, 33.2, 39.8, and 58.9° can be indexed to (002), (100), (103), and (110) crystal planes of 2H-MoS_2 (JCPDS 37-1492), respectively. While the peak position of the patterns with surfactant is similar to that of the sample without surfactant. The results indicate that the crystalline structure of molybdenum disulfide is not affected by the introduction of surfactant. However, the intensity of all diffraction peaks was weakened after surfactants were added, with peak (002) showing the greatest reduction, implying that the crystallization of molybdenum disulfide was reduced by the addition of surfactants. The intensity of the diffraction peak (002) demonstrates a noteworthy decrease, suggesting that the addition of surfactants impedes the development of the molybdenum disulfide layer structure.[23] The spacing between

https://doi.org/10.1021/acsomega.3c10031
ACS Omega 2024, 9, 9792−9802

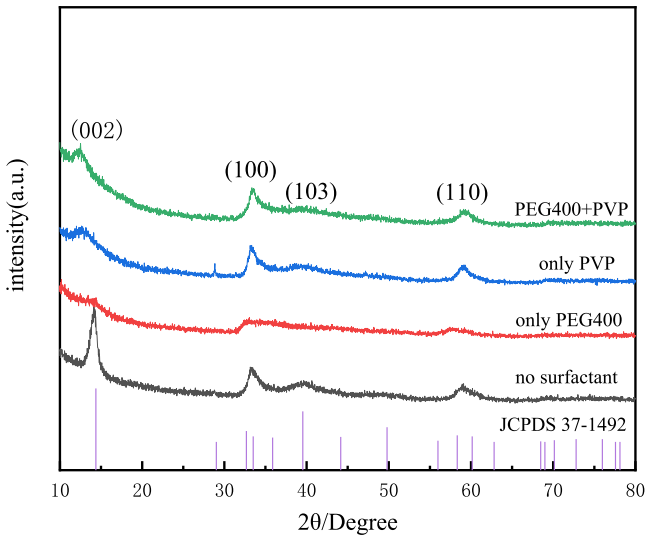

Figure 2. XRD patterns of MoS_2 and NMC synthesized with different surfactants.

the adjacent (002) crystal planes can be calculated by the Bragg eq (eq 1).

$$2d\sin\theta = n\lambda \quad (1)$$

where d represents the distance between crystal planes, θ is the diffraction degree, n is the diffraction order, and λ is the X-ray wavelength (λ = 0.15406 nm for Cu target *K*a radiation). As per the equation, a shift of the (002) peak to a lower degree indicates an increase in the distance between the (002) crystal planes. As shown in Figure 2, the (002) peak position of MoS_2 without surfactant is approximately 13.9°, which shifts to a lower degree with surfactant. With the addition of PEG400, the intensity of the (002) peak decreased notably and shifted to roughly 13.6°. As for the PVP addition, the (002) peak shifted further leftward to 12.5°. When both surfactants were added simultaneously, the (002) peak shifted to around 12.2°, which is lower by approximately 1.7°, compared to the pristine MoS_2. As a result, the introduction of surfactants enhances the interlayer spacing of MoS_2.

Molybdenum disulfide synthesized with PEG400 and PVP as synergistic surfactant was annealed at 500, 700, and 900 °C for 2 h, respectively. Figure 3 shows the FESEM images of the samples after annealing at different temperatures. The morphology of molybdenum disulfide does not change significantly before and after annealing, indicating that high-temperature treatment has little effect on the morphology of the specimens. Point scanning energy spectrum analysis was conducted at point m (unannealed) in Figure 3a and point n (annealed) in Figure 3c, and the EDS maps were obtained, as shown in Figure 4. It is evident from the figure that the main elements of the samples prior to and postannealing are C, O, S, and Mo. The atomic ratio of S to Mo before and after annealing is 18.23:9.26 and 28.61:14.81, respectively, which is approximately 2:1. Hence, it can be proven that the main phase of the as-prepared samples is MoS_2, which is also identified by XRD analysis. The C element mainly originates from the residue of the surfactant. EDS analysis revealed a decline in the mass fraction of C and O elements in molybdenum disulfide after annealing at 700 °C for 2 h. This implies that some of the carbon is lost as gaseous oxides during the high-temperature treatment process. Nevertheless, not all carbon is eliminated

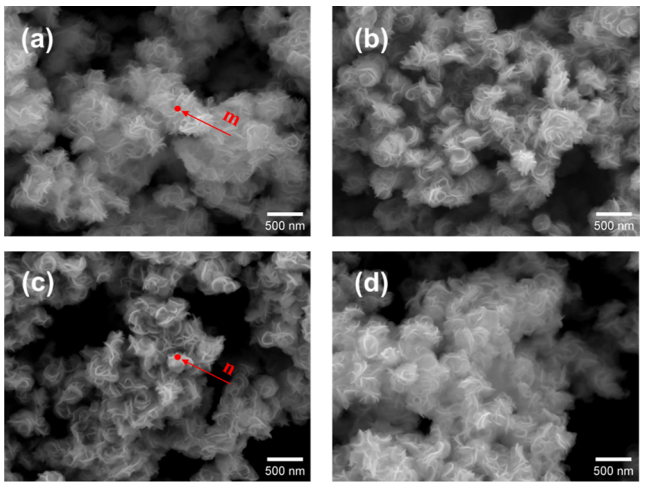

Figure 3. FESEM images of NMC before and after annealing (a, unannealed; b, 500 °C; c, 700 °C; d, 900 °C).

since the residual PEG400 and PVP carbonizes to form amorphous carbon, which is uniformly distributed in molybdenum disulfide. The reduction of O content is caused by the decomposition of oxygen-containing functional groups on surfactants at high temperatures and the volatilization with carbon.

Figure 5 shows the XRD patterns of the NMC samples before and after annealing. Four diffraction peaks located at 2θ of 13.9, 33.2, 39.7, and 58.8° represent the (002), (100), (103), and (110) crystal plane of 2H-MoS_2 respectively (JCPDS 37-1492). As displayed in Figure 5, the intensity of the (100), (102), and (110) diffraction peaks increased after high-temperature treatment, denoting the high crystallinity of the specimens. Interestingly, the intensity of the diffraction peak (002) decreased at elevated temperatures, suggesting inhibited layered stacking of molybdenum disulfide. The reduced layered structure can be attributed to the super-abundant defects in the structure caused by the high-temperature treatment.[29] Nevertheless, the XRD patterns obtained after annealing at 700 and 900 °C exhibit very little disparity, indicating that the crystal structure of molybdenum disulfide will not be further affected when the annealing temperature exceeds 700 °C.

Figure 6 shows the XPS spectra of the NMC samples before and after annealing. The survey spectra (shown in Figure 6a) demonstrate that the samples both prior to and postannealing consist mainly of Mo, S, C, N, and O elements. The O element is mainly derived from both oxygen adsorption and oxygen-containing functional groups in surfactants. The C and N elements primarily originate from surfactant residues. Figure 6b,c displays Mo 3d spectra of NMC before and after annealing. As shown in Figure 6b, prior to annealing, the Mo 3d spectrum shows five distinct peaks, where the Mo^{4+} $3d_{5/2}$ and Mo^{4+} $3d_{3/4}$ peaks (at 229.37 and 232.47 eV, respectively) correspond to the molybdenum ion of 2H-MoS_2. The Mo^{4+} $3d_{5/2}$ peak at 229.37 eV also displays a small peak toward the lower binding energy. This peak observed at 228.40 eV indicates the presence of a small quantity of 1T phase molybdenum disulfide in the synthesized material.[30] Meanwhile, the peaks at 226.43 and 235.66 eV correspond to S 2s and Mo^{6+} $3d_{5/2}$, where the latter is derived from the M−O bond of MoO_3. It is speculated that molybdenum oxide results from the incomplete reaction, leaving a small amount of MoO_3

https://doi.org/10.1021/acsomega.3c10031
ACS Omega 2024, 9, 9792−9802

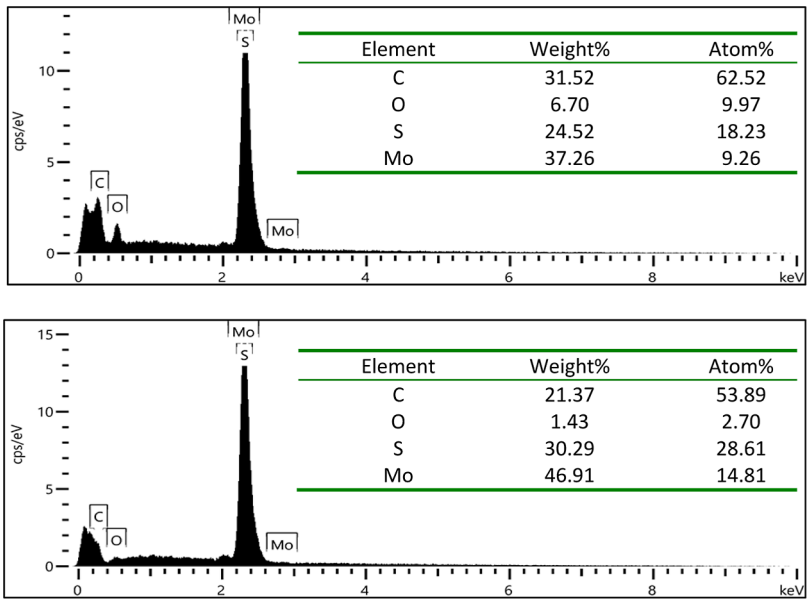

Figure 4. EDS maps of NMC before and after annealing.

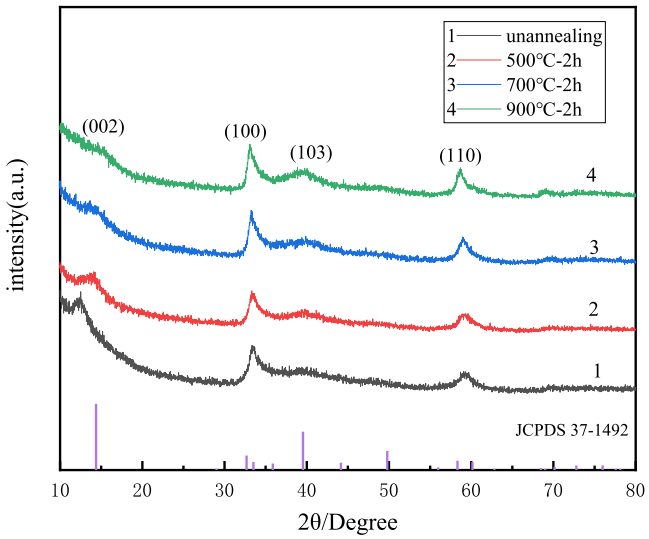

Figure 5. XRD patterns of N-doped MoS_2/C composites before and after annealing.

in the final product. Further, MoS_2 is oxidized by residual oxygen molecules absorbed on the surface to generate molybdenum oxide during calcination.[31]

Figure 6c shows the Mo 3d spectrum of NMC after roasting. The peaks at 229.82 and 232.95 eV correspond to Mo^{4+} $3d_{5/2}$ and Mo^{4+} $3D_{3/4}$, respectively. After annealing, the small peak at 229.37 eV present in the precalcined sample was absent. This indicates the complete conversion of metastable 1T-MoS_2 to 2H-MoS_2 during the annealing procedure. A considerable decrease was noted in the intensity and area of the Mo^{6+} $3d_{5/2}$ peak at 235.50 eV as contrasted to the values before roasting. The findings suggest that the majority of MoO_3 has sublimed, leaving a small fraction behind during annealing. Consequently, the content of Mo^{6+} declined in the sample. Figure 6d,e illustrates the S 2P spectra, which depict the valence states of the molybdenum disulfide before and after annealing. Both samples exhibit two peaks, S^{2-} $2p_{3/2}$ and S^{2-} $2p_{1/2}$, which appear at 162.19 and 163.47 eV before annealing in Figure 6d, while at 162.24 and 163.84 eV after calcination in Figure 6e. Figure 6f displays the C 1s spectrum of the NMC prior to annealing. The peak at 284.65 eV corresponds to the C−C bond, which originates from the residual carbon chains of PEG400 and PVP. The peaks at 286.01 and 288.05 eV correspond to C−N and C═O bonds, respectively, and are derived from residual PVP. Figure 6g displays the C 1s spectrum of the specimen following a high-temperature treatment. The unheated sample exhibits three discernible peaks at 284.76, 286.1, and 288.57 eV, respectively, which corresponded to C−C, C−N, and C═O bonds, respectively.[32] While the peak position relating to C−C bonds remained relatively stable, in contrast, those linked to C−N and C═O bonds experienced significant peak area reductions.

According to the data presented in Table 1, the atomic ratio of C−N decreased from 14.48 to 10.77%, and C═O reduced from 6.06 to 2.30% after annealing. The surfactant within molybdenum disulfide was carbonized during roasting, resulting in the retention of most C−C bonds and the near-complete sublimation of pyrrole at 700 °C. Consequently, the C═O content was reduced to a minimum, while the N element attached to the carbon chain was partially preserved. Figure 6h,i shows the N 1s spectra of the as-prepared sample prior to and postannealing. It can be observed from Figure 6h that two peaks appear at 395.2 and 399.84 eV, corresponding to Mo $3p_{3/2}$ and Pyrrolic N, respectively.[33] Pyrrole N is derived from polyvinylpyrrolidone (PVP). After annealing, the spectrum of N 1s reveals two peaks indicative of Mo 3p3/2 and Pyrrolic N at 395.69 and 399.64 eV, respectively, as shown in Figure 6i. Compared with samples prior to annealing, the pyrrole N content of samples after annealing is greatly reduced. Table 1 illustrates a 3.49% decrease in the atomic ratio of pyrrole N, declining from 10.12 to 6.63% after annealing, which is consistent with the reduction rate of the C−N bond. Thus, the experiment validates both the regulation of morphology and the achievement of N element doping into the MoS_2/C composites. During the carbonization of the carbon chain in PVP, the N element distributes uniformly in molybdenum disulfide together with the carbon chain. N^{3-} ions (0.171 nm) have a similar ionic radius to S^{2-} ions (0.184

https://doi.org/10.1021/acsomega.3c10031
ACS Omega 2024, 9, 9792−9802

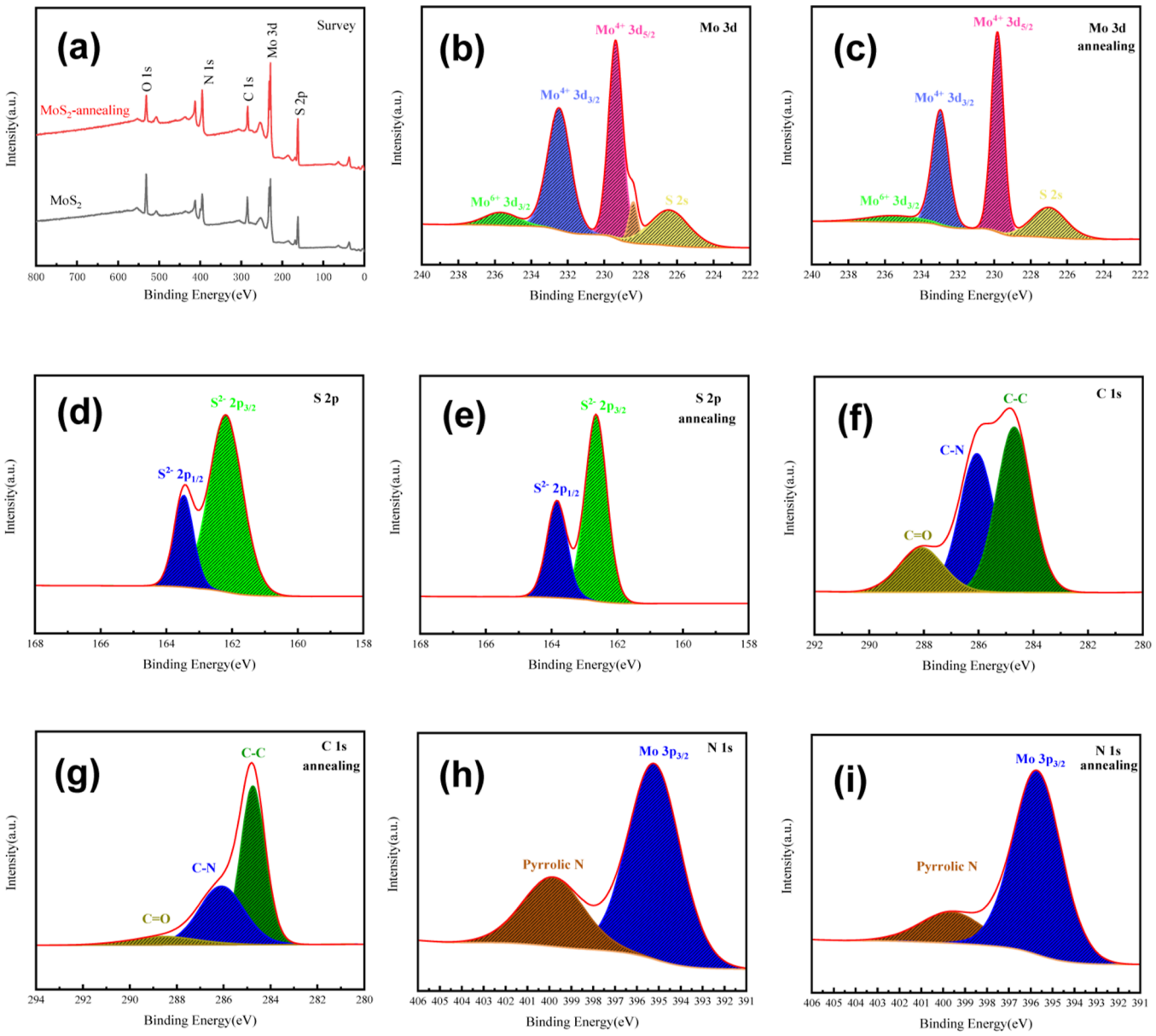

Figure 6. XPS spectra of NMC before and after annealing (a, survey spectra before and after annealing; b, Mo 3d before annealing; c, Mo 3d after annealing; d, S 2p before annealing; e, S 2p after annealing; f, C 1s before annealing; g, C 1s after annealing; h, N 1s before annealing; i, N 1s after annealing).

Table 1. C 1s and N 1s Spectrogram Atomic Ratio of NMC Before and After Annealing

type	before annealing	after annealing
C−C	17.78%	15.87%
C−N	14.48%	10.77%
C═O	6.06%	2.30%
Mo $3p_{3/2}$	24.58%	30.01%
Pyrrolic N	10.15%	6.63%

nm) but possess different valence states. Therefore, doping the N element into the lattice of MoS_2 introduces defects and enhances the conductivity of MoS_2.

Figure 7 depicts the HRTEM images for NMC samples prior to annealing in (a) and (b) and after annealing in (c) and (d). It can be observed that the morphology of NMC retains a flower-like structure composed of molybdenum disulfide nanosheets without any significant change after annealing. Figure 7b shows an HRTEM image (400,000×) of several few-layered ultrathin MoS_2 nanosheets, each composed of only five or nine layers. The results show that the layer growth of the (002) crystal plane is inhibited, which is consistent with the XRD analysis. Using Fourier transform and DigitalMicrograph software, the spacing of the (002) crystal plane after annealing was determined to be 0.67 nm. After annealing, the crystal plane spacing increased by more than 0.64 nm. This was attributed to the carbonization of residual surfactants remaining in molybdenum disulfide. Consequently, molybdenum disulfide can fully contact the electrolyte. Figure 7d shows that the lattice fringe of the roasted molybdenum disulfide exhibits more bending and discontinuity compared to the unannealed samples. This suggests that a high-temperature environment has resulted in the formation of more defects,[34] which in turn can provide more impingement sites for lithium

https://doi.org/10.1021/acsomega.3c10031
ACS Omega 2024, 9, 9792−9802

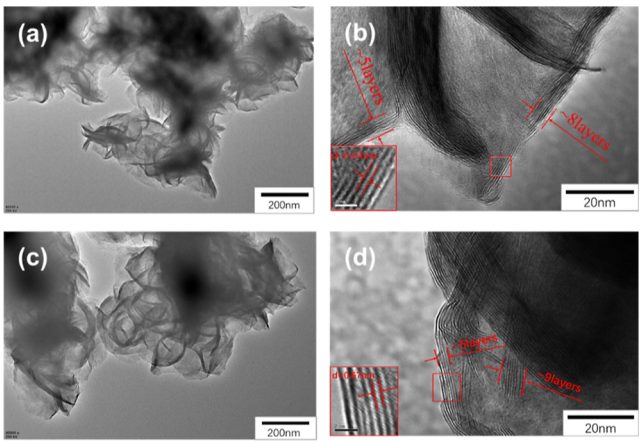

Figure 7. HRTEM images of NMC before and after annealing (a, before annealing, 50,000×; b, before annealing, 400,000×; c, after annealing at 700 °C, 50,000×; d, after annealing at 700 °C, 400,000×).

ions and enhance the specific capacity. Furthermore, the enhanced spacing between layers can effectively buffer the expansion of the volume during the charging and discharging process, leading to an improvement in stability.

3.2. Analysis of Hydrothermal Synthesis Mechanism. According to characterization results in the previous sections, it is inferred that the reaction mechanism is as depicted in Figure 8. At the initial stage of the reaction, the molybdate ions in solution were attracted to the hydrophilic −*O*− bond on the carbon chain of PEG400 and bound to it as a "surface template" to determine their growth position.[35] Subsequently, driven by a hydrophilic amide group and a hydrophobic alkyl backbone, PVP self-assembled spontaneously into vesicular micelles with amide groups outside and alkyl backbone chains inside, as reported by ref 36. The nucleation cores of MoS_2 were then enclosed in the solution, forming a circular "microreactor".[37,38] The MoS_2 nanosheets grew directionally in a specific region of the "microreactor" that serves as a "bottom template" to limit its growth space. In this manner, uniformly dispersed nanoflower-like MoS_2 with an average grain size of approximately 500 nm was generated. Excessive PEG400 molecules were driven by hydrophilic and hydrophobic groups alternatively to form micellar aggregates,[39] which were dispersed into the solution to prevent the MoS_2 nuclei from aggregating contact due to the steric hindrance effect. Thus, the morphology of MoS_2 was transformed into microspheres, and the agglomeration was reduced simultaneously. Then, the hydrothermal product was annealed for two h with a nitrogen atmosphere at 700 °C. After annealing, the surfactant remaining in molybdenum disulfide was carbonized, while the N element connected to the carbon chain via a C−N bond was retained. Finally, N-doped nanoflower-like MoS_2/C composites were synthesized.

3.3. Electrochemical Performance. Figure 9a displays the cyclic voltammetry (CV) curves of NMC samples after calcination, performed at a scan rate of 0.3 $mV{\cdot}s^{-1}$ in a potential range of 0.01−3 V. The figure shows two reduction peaks at 0.79 and 0.45 V during the first cathodic scan. The reduction peak at 0.79 V represents the intercalation process where Li^+ is embedded in the MoS_2 layer to form a compound, accompanied by a phase transition of MoS_2 from 2H to 1T.[40] The reaction equation for the intercalation of lithium ions with MoS_2 is $xLi^+ + xe^- + MoS_2 \rightarrow Li_xMoS_2$. However, the reduction peak at 0.45 V represents the transition of the intercalation compound Li_xMoS_2 to the metallic molybdenum and Li_2S. The reaction equation for this transition is $Li_xMoS_2 + (4 - x)Li^+ + (4 - x)e^- \rightarrow Mo + 2Li_2S$. Furthermore, the reaction between lithium ions and electrolytes results in a solid electrolyte interface film (SEI film). The first anodic scan displays two oxidation peaks at 1.68 and 2.28 V. The oxidation peak at 1.68 V corresponds to the partial conversion of Mo to MoS_2, as indicated by the following reaction equation: $Li_xMoS_2 \rightarrow MoS_2 + x\ Li^+ + S + x\ e^-$. The oxidation peak at 2.28 V represents the conversion of Li_2S to S, with the equation: $Li_2S\text{-}2e^- \rightarrow 2Li^+ + S$. The second cathodic scan in the subsequent cycle exhibits two reduction peaks, indicating that the reaction of the second cathodic scan was identical to that of the first scan. Specifically, it involved the transformation of MoS_2 to metallic Mo nanoparticles and Li_2S. Nonetheless, the position of the reduction peak differs from the first cycle, appearing at 1.92 and 1.06 V. This deviation is due to the consumption of a portion of lithium ions in the irreversible reaction that occurs during the SEI film formation in the first cycle.[41,42] The comparable CV curves in the second and third cycles confirm that the material exhibits excellent stability and reversibility.

Figure 9b shows the charge/discharge profiles of N-doped MoS_2/C material after annealing at 700 °C for 2 h. The testing was performed at a current density of 500 $mA{\cdot}g^{-1}$, with a

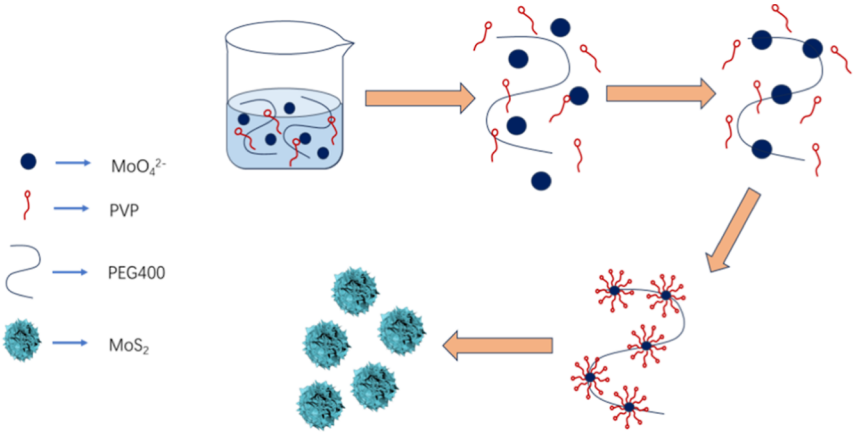

Figure 8. Illustration of the synthesis mechanism of NMC.

https://doi.org/10.1021/acsomega.3c10031
ACS Omega 2024, 9, 9792−9802

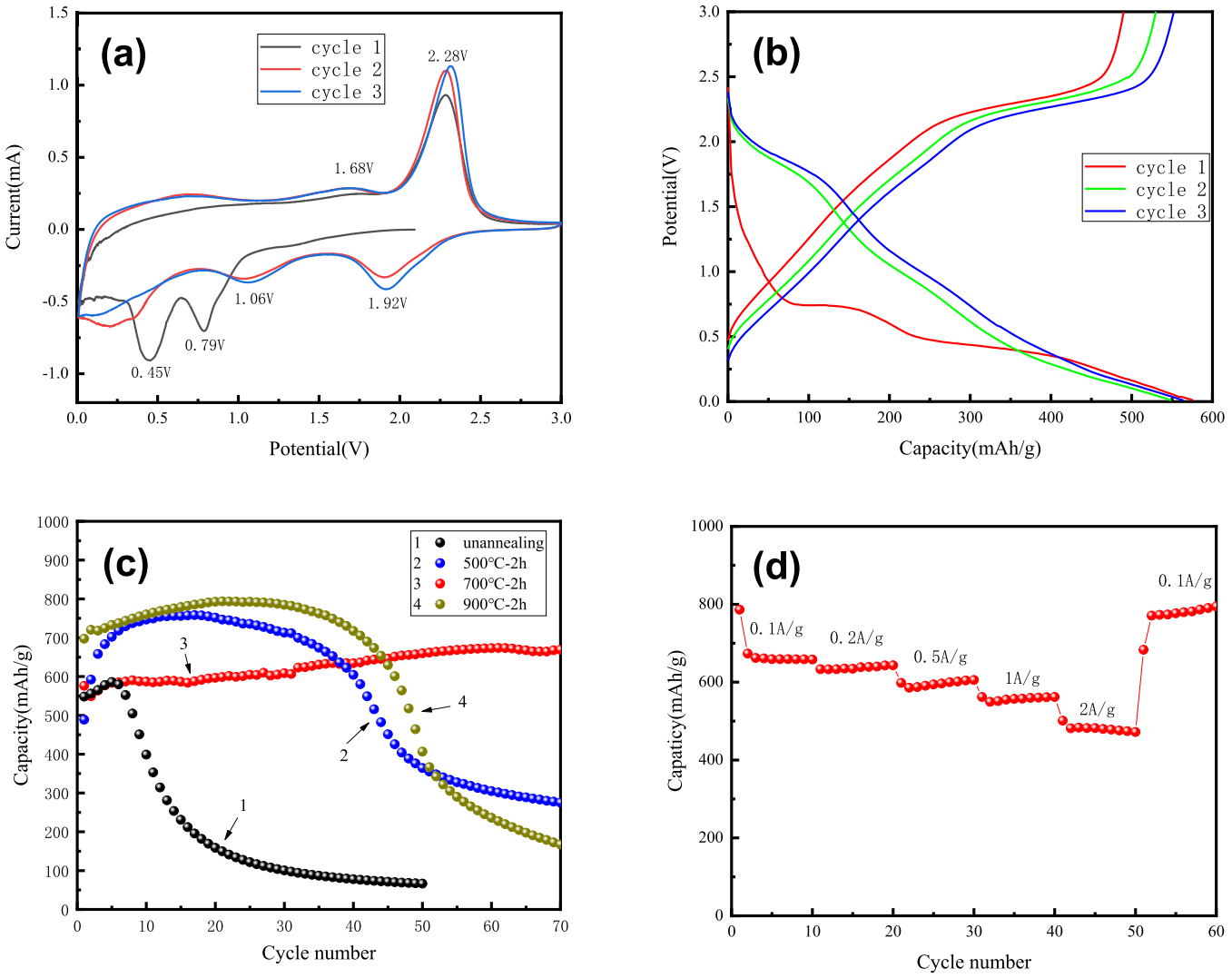

Figure 9. Electrochemical property of NMC (a, CV curves; b, charge and discharge curves of the first three turns; c, cycle charge and discharge curves; d, rate curve).

voltage range of 0.01−3 V for the first three cycles. The first discharge curve reveals two voltage platforms at 0.75 and 0.47 V. The voltage platform at 0.75 V denotes the insertion of Li^+ ions between the MoS_2 layers to form the intercalation compound Li_xMoS_2. The voltage platform observed at 0.47 V suggests that the intercalation compound transforms into Mo nanoparticles and Li_2S. In the first charge curve, a voltage platform appears between 2.18 and 2.4 V, representing the transformation of Li_2S to S. The voltage platforms correspond distinctly with the REDOX peaks observed in the cyclic voltammetry (CV) curves. However, a slight discrepancy still exists and may be related to the battery manufacturing process. Nevertheless, the second and third charge/discharge curves display notable differences from the initial ones. This is attributed to the irreversible reaction of lithium ions with the electrolyte, resulting in the formation of the SEI film during the first discharge. Consequently, certain lithium ions are permanently lost, leading to inconsistencies between the first scan and the following two scans of the CV curves.

The N-doped MoS_2/C specimens after annealing at 500, 700, and 900 °C, respectively, for two h were assembled into button batteries. The charge−discharge cyclic performance of the material was tested at a current density of 500 $mA{\cdot}g^{-1}$, as shown in Figure 9c. It is apparent that the specific discharge capacity of the sample before roasting was 548.2 $mA{\cdot}g^{-1}$ for the first cycle. Although the capacity increased over the next five cycles, it dramatically declined after the fifth. By the 50th cycle, the specific discharge capacity had decreased to just 66.4 $mA{\cdot}g^{-1}$, with a capacity retention rate of only 12%. Annealing at elevated temperatures is a potential solution to enhance cycle capacity and stability. Samples annealed at 700 °C for 2 h demonstrated the best performance with an initial specific discharge capacity of 575.9 $mA{\cdot}g^{-1}$ and a gradual increase in the subsequent 70 cycles. After the 70th cycle, the specific discharge capacity reached 669.2 $mA{\cdot}g^{-1}$, while also maintaining a capacity retention rate of 116%. Therefore, annealing is essential for the cyclic performance of the as-prepared materials. The annealing treatment both benefits the crystallinity of the material and facilitates the carbonization of surfactant remaining in molybdenum disulfide. N-doped MoS_2/C composites were synthesized by the doping of N elements, resulting in improved conductivity and enhanced electron transport. Moreover, the layer spacing of the plane (002) was found to increase after annealing, leading to more contact sites for lithium ions and providing a buffer for volume expansion during the charge/discharge cycles. Consequently,

https://doi.org/10.1021/acsomega.3c10031
ACS Omega 2024, 9, 9792−9802

the cycle performance of N-doped MoS_2/C composites was significantly improved.

During the first 30 cycles, the specific discharge capacity of the sample exhibited a substantial increase after roasting at 500 and 900 °C for 2 h. Nevertheless, the capacity retention rate was subpar, plummeting significantly after the 40th cycle. The sample treated at 500 °C demonstrated an initial specific discharge capacity of 488.7 mA·g^{-1}, which dropped to 275.2 mA·g^{-1} with a capacity retention rate of 56% on the 70th cycle. The initial specific discharge capacity of the sample treated at 900 °C was 697.4 mA·g^{-1}, which is the highest in the three samples. However, it decreased to 167.2 mA·g^{-1} in the following 70th cycle with a capacity retention rate of only 24%. In comparison to the samples treated at 700 °C, these values were notably lower. Thus, the optimal roasting temperature for the hydrothermal product was found to be 700 °C.

The rate performance of the NMC samples annealed at 700 °C for 2 h was evaluated by cycling 10 times at each current density, as illustrated in Figure 9d. The discharge specific capacity of the NMC is 658.9, 634.3, 596.5, 557.5, and 479.7 mA·g^{-1} at current densities of 0.1, 0.2, 0.5, 1, and 2 A·g^{-1}, respectively. The material exhibits excellent tolerance for changes in the current density. As the current density increases, there is only a slight decrease in the specific discharge capacity. Even at a high current density of 2 A·g^{-1}, it still has a specific discharge capacity of 479.7 mA·g^{-1}. When the current density drops to 0.1 A·g^{-1}, the specific discharge capacity rises to 770.6 mA·g^{-1}. Additionally, during the rate performance test, the specific discharge capacity exhibits a consistent upward trend. This is due to the fact that at lower current densities, electrons, and ions are transported more smoothly within the electrode material, resulting in increased reactivity. And as the current density decreases, the electrolyte ions have more time to redistribute in the electrode material, resulting in an increase in the specific discharge capacity. The discharge plateau is longer and smoother when the current density drops back to 0.1 A·g^{-1}. This results in an increase in the specific discharge capacity. The initial discharge specific capacity was 786 mA·g^{-1}, and the discharge specific capacity was 794.1 mA·g^{-1} at the end of the rate performance test. The capacity increases by 1% compared to the initial discharge specific capacity, which is consistent with the cyclic performance diagram shown in Figure 9c.

The specimens before and after annealing were first cycled 10 times at a current density of 500 A·g^{-1} and subsequent take measurements of electrochemical impedance spectroscopy (EIS). The Nyquist diagram (Figure 10a) was obtained by analog circuit fitting in Zview software. As depicted in Figure 10a, each curve exhibits two distinct formations: a semicircle in the high-frequency region and a slash in the low-frequency region. The initial point of the high-frequency semicircle on the Z' axis is not zero, indicating the presence of an electrolyte resistance Rs. The high-frequency semicircle represents the charge transfer resistance Rct between the electrode and the electrolyte. CPE is the constant phase element. The slanted line in the low-frequency region represents the Warburg impedance Zw, also recognized as the concentration polarization impedance, that occurs due to the impact of reactant concentration and diffusion on the electrode reaction.[43] The equivalent circuit diagram is presented in Figure 10b. The Nyquist diagram in Figure 10a illustrates that the Rct of the pristine MoS_2 material is 333.5 Ω, while the Rct of the N-doped MoS_2/C material is 240.8 Ω. Remarkably, the Rct of

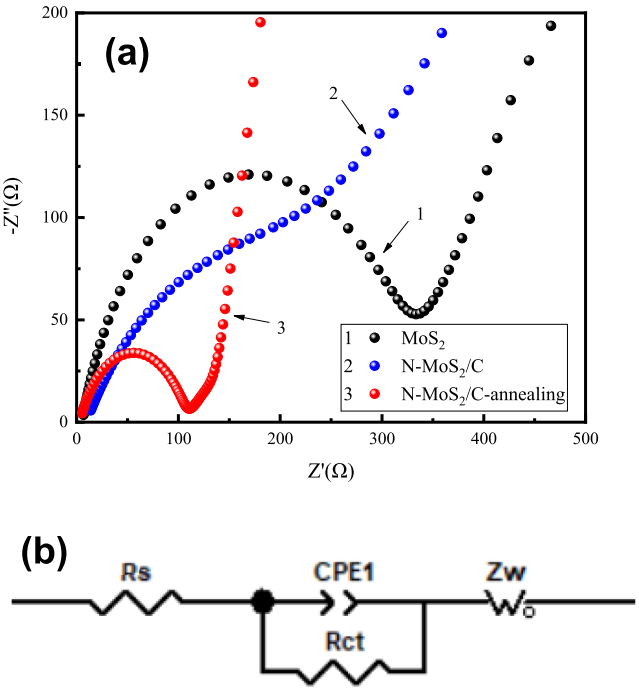

Figure 10. (a) Nyquist diagram of NMC before and after annealing and (b) equivalent circuit diagram.

NMC annealing at 700 °C for two h significantly drops to 108.6 Ω, which is the smallest value among the specimens. The results demonstrate that NMC after annealing have excellent charge transport performance and lithium ion diffusion performance. Specifically, MoS_2 was doped with N and integrated with carbon, resulting in increased conductivity and a significantly enhanced electrochemical performance.

4. CONCLUSIONS

Nanocrystalline flower-like N-doped MoS_2/C composites were synthesized by an enhanced hydrothermal method, utilizing sodium molybdate as a source of molybdenum and thiourea as a source of sulfur. Surfactants, including polyethylene glycol 400 (PEG400) and polyvinylpyrrolidone (PVP) were employed in the hydrothermal reaction as soft template surfactants and nitrogen sources. After annealing in an argon atmosphere at 700 °C for 2 h, the hydrothermal residue transformed into N-doped MoS_2/C composites, as the residual surfactant was carbonized while retaining the N element during the annealing procedure. The as-prepared N-doped MoS_2/C composites with an average particle size of approximately 500 nm were uniformly dispersed without agglomeration. No morphological changes were observed before and after annealing. The initial specific discharge capacity of the N-doped MoS_2/C composite was 548.2 mA·g^{-1} without annealing. However, the specific discharge capacity dropped significantly to 66.4 mA·g^{-1} by the 50th cycle, exhibiting a capacity retention rate of only 12%. In contrast, the initial specific discharge capacity of the samples after annealing was 575.9 mA·g^{-1}. Furthermore, there was a noticeable increase in the discharge capacity throughout the cycles, with a discharge specific capacity of 669.2 mA·g^{-1} by the 70th cycle. The capacity retention rate reached an impressive 116%, leading to a significantly improved cycle performance. Additionally, the impedance of the N-doped MoS_2/C composites was reduced

https://doi.org/10.1021/acsomega.3c10031
ACS Omega 2024, 9, 9792−9802

after annealing, resulting in a promoted electron/ion transfer at the electrode interface. This study manifests that the design of hybrid materials and carbonization at high temperatures can significantly modify the electrochemical performance of molybdenum disulfide as an anode material for lithium-ion batteries and also provides new research ideas for the application of other layered materials in energy storage devices.

AUTHOR INFORMATION

Corresponding Author

Wei Liu − *School of Material Science and Engineering, Henan University of Science and Technology, Luoyang 471023, China; Collaborative Innovation Center for New Materials and Advanced Processing Technologies of Nonferrous Metals, Luoyang 471023, China;* orcid.org/0009-0003-0773-201X; Email: liuwei@haust.edu.cn

Authors

Shenshen Yang − *School of Material Science and Engineering, Henan University of Science and Technology, Luoyang 471023, China; Henan University of Science and Technology National Joint Engineering Research Center for Abrasion Control and Molding of Metal Materials, Luoyang 471003, China*

Dongsheng Fan − *School of Material Science and Engineering, Henan University of Science and Technology, Luoyang 471023, China; Henan University of Science and Technology National Joint Engineering Research Center for Abrasion Control and Molding of Metal Materials, Luoyang 471003, China*

Yang Wu − *School of Material Science and Engineering, Henan University of Science and Technology, Luoyang 471023, China*

Jingbo Zhang − *School of Material Science and Engineering, Henan University of Science and Technology, Luoyang 471023, China; Henan University of Science and Technology National Joint Engineering Research Center for Abrasion Control and Molding of Metal Materials, Luoyang 471003, China*

Yaozong Lu − *School of Material Science and Engineering, Henan University of Science and Technology, Luoyang 471023, China; Henan University of Science and Technology National Joint Engineering Research Center for Abrasion Control and Molding of Metal Materials, Luoyang 471003, China*

Linping Fu − *School of Material Science and Engineering, Henan University of Science and Technology, Luoyang 471023, China; Henan University of Science and Technology National Joint Engineering Research Center for Abrasion Control and Molding of Metal Materials, Luoyang 471003, China*

Complete contact information is available at: https://pubs.acs.org/10.1021/acsomega.3c10031

Notes

The authors declare no competing financial interest.

ACKNOWLEDGMENTS

This work is supported by the National Natural Science Foundation of China (no. U1404511), Henan Province Science and Technology R&D Program Joint Fund Project (no.222103810038), Henan Province Higher Education Schools Youth Backbone Teacher Training Program(2019GGJS073) and Henan Provincial University Key Research Project (no.24B430007).

REFERENCES

(1) Cheng, H.; Shapter, J. G.; Li, Y.; Gao, G. Recent progress of advanced anode materials of lithium-ion batteries. *J. Energy Chem.* **2021**, *57*, 451−468.

(2) Zhang, Y.; Zhou, Q.; Zhu, J.; Yan, Q.; Dou, S. X.; Sun, W. Nanostructured Metal Chalcogenides for Energy Storage and Electrocatalysis. *Adv. Funct. Mater.* **2017**, *27* (35), 1702317.

(3) Weitemeyer, S.; Kleinhans, D.; Vogt, T.; Agert, C. Integration of Renewable Energy Sources in future power systems: The role of storage. *Renewable Energy* **2015**, *75*, 14−20.

(4) Xu, H.; Li, H.; Wang, X. The Anode Materials for Lithium-Ion and Sodium-Ion Batteries Based on Conversion Reactions: a Review. *ChemElectroChem* **2023**, *10* (9), No. e202201151.

(5) Armand, M.; Tarascon, J. M. Building better batteries. *nature* **2008**, *451* (7179), 652−657.

(6) Kumar, R.; Sahoo, S.; Joanni, E.; Singh, R. K.; Tan, W. K.; Kar, K. K.; Matsuda, A. Recent progress in the synthesis of graphene and derived materials for next generation electrodes of high performance lithium ion batteries. *Prog. Energy Combust. Sci.* **2019**, *75*, 100786.

(7) Tarascon, J. M.; Armand, M. Issues and challenges facing rechargeable lithium batteries. *nature* **2001**, *414* (6861), 359−367.

(8) Yoshino, A. The Birth of the Lithium-Ion Battery. *Angew. Chem., Int. Ed.* **2012**, *51* (24), 5798−5800.

(9) Zubi, G.; Dufo-López, R.; Carvalho, M.; Pasaoglu, G. The lithium-ion battery: State of the art and future perspectives. *Renewable Sustainable Energy Rev.* **2018**, *89*, 292−308.

(10) Li, W.; Liu, Y.; Zheng, S.; Hu, G.; Zhang, K.; Luo, Y.; Qin, A. Hybrid Structures of Sisal Fiber Derived Interconnected Carbon Nanosheets/MoS_2/Polyaniline as Advanced Electrode Materials in Lithium-Ion Batteries. *Molecules* **2021**, *26* (12), 3710.

(11) Long, F.; Chen, Y.; Wu, C.; Wang, J.; Mo, S.; Zou, Z.; Zheng, G. Unique three-dimensional hierarchical heterogeneous MoS_2/graphene structures as a high-performance anode material for lithium-ion batteries. *Ionics* **2021**, *27*, 1977−1986.

(12) Liu, Z.; Xiao, D.; Huang, H.; Zhang, J.; Niu, C. Carve designs of MoS_2 nanostructures by controlling 3D MoS_2 nanomasks. *Inorg. Chem. Front.* **2018**, *5* (10), 2598−2604.

(13) Choi, J.-H.; Kim, M.-C.; Moon, S.-H.; Kim, H.; Kim, Y. S.; Park, K. W. Enhanced electrochemical performance of MoS_2/graphene nanosheet nanocomposites. *RSC Adv.* **2020**, *10* (32), 19077−19082.

(14) Zhang, R.; Qin, Y.; Liu, P.; Jia, C.; Tang, Y.; Wang, H. How does Molybdenum Disulfide Store Charge: A Minireview. *ChemSusChem* **2020**, *13* (6), 1354−1365.

(15) Zhao, J.; Zhang, Y.; Wang, Y.; Li, H.; Peng, Y. The application of nanostructured transition metal sulfides as anodes for lithium ion batteries. *J. Energy Chem.* **2018**, *27* (6), 1536−1554.

(16) Zhao, L.; Wang, Y.; Wei, C.; Huang, X.; Zhang, X.; Wen, G. MoS_2-based anode materials for lithium-ion batteries: Developments and perspectives. *Particuology* **2024**, *87*, 240−270.

(17) Liu, M.; Li, N.; Wang, S.; Li, Y.; Liang, C.; Yu, K. 3D nanoflower-like MoS_2 grown on wheat straw cellulose carbon for lithium-ion battery anode material. *J. Alloys Compd.* **2023**, *933*, 167689.

(18) Liu, D.; Lv, Z.; Dang, J.; Ma, W.; Jian, K.; Wang, M.; Huang, D.; Tian, W. Nitrogen-Doped MoS2/Ti_3C_2T X Heterostructures as Ultra-Efficient Alkaline HER Electrocatalysts. *Inorg. Chem.* **2021**, *60* (13), 9932−9940.

(19) Jiang, J.; Zhang, Y.; An, Y.; Wu, L.; Zhu, Q.; Dou, H.; Zhang, X. Engineering ultrathin MoS_2 nanosheets anchored on N-doped carbon microspheres with pseudocapacitive properties for high-performance lithium-ion capacitors. *Small Methods* **2019**, *3* (7), 1900081.

(20) Cao, X.; Chen, Z.; Wang, N.; Han, Z.; Zheng, X.; Yang, R. Defected molybdenum disulfide catalyst engineered by nitrogen doping for advanced lithium−oxygen battery. *Electrochim. Acta* **2021**, *383*, 138369.

(21) Li, S.; Qu, D.; Wang, P.; Wang, Y.; Xie, F. N-doped MoS2 Nano-Flowers as High-Performance Anode Electrode for Excellent Lithium Storage. *Int. J. Electrochem. Sci.* **2019**, *14* (8), 7507−7515.
(22) Feng, N.; Meng, R.; Zu, L.; Feng, Y.; Peng, C.; Huang, J.; Liu, G.; Chen, B.; Yang, J. A polymer-direct-intercalation strategy for MoS_2/carbon-derived heteroaerogels with ultrahigh pseudocapacitance. *Nat. Commun.* **2019**, *10* (1), 1372.
(23) Yin, M.; Song, H.; Tang, A.; Xu, G.; Liu, L.; Pan, Y. Effect of carbon sources on morphologies and electrochemical properties of MoS_2/carbon composites. *Ionics* **2019**, *25*, 2087−2092.
(24) Luo, X.; Li, N.; Guo, X.; Wu, K. One-pot hydrothermal synthesis of MoS_2 anchored corncob-derived carbon nanospheres for use as a high-capacity anode for reversible Li-ion battery. *J. Solid State Chem.* **2021**, *296*, 122020.
(25) Ma, W.; Zhang, X.; Meng, Y.; Zhao, J. Hierarchical carbon/MoS_2 composites as anodes for advanced electrochemical performance. *Ionics* **2022**, *28* (12), 5499−5504.
(26) Shi, Y. H.; Li, X. Y.; Zhang, W. D.; Li, H. H.; Wang, S. G.; Wu, X. L.; Su, Z. M.; Zhang, J. P.; Sun, H. Z. Micron-scaled MoS_2/N-C particles with embedded nano-MoS_2: A high-rate anode material for enhanced lithium storage. *Appl. Surf. Sci.* **2019**, *486*, 519−526.
(27) Gu, P.; Zhao, C.; Wen, T.; Ai, Y.; Zhang, S.; Chen, W.; Wang, J.; Hu, B.; Wang, X. Highly U(VI) immobilization on polyvinyl pyrrolidine intercalated molybdenum disulfide: Experimental and computational studies. *Chem. Eng. J.* **2019**, *359*, 1563−1572.
(28) Liu, Y.; Zhang, L.; Wang, H.; Yu, C.; Yan, X.; Liu, Q.; Xu, B.; Wang, L. m. Synthesis of severe lattice distorted MoS_2 coupled with hetero-bonds as anode for superior lithium-ion batteries. *Electrochim. Acta* **2018**, *262*, 162−172.
(29) Zhu, W.; Shi, C.; Zhao, J.; Wang, Y.; Hu, Y. Structure and electrochemical performance of MoS_2 based on different molybdenum-sulfur mole ratios. *J. Phys. Chem. Solids* **2022**, *167*, 110749.
(30) Wang, J.; Fang, W.; Hu, Y.; Zhang, Y.; Dang, J.; Wu, Y.; Zhao, H.; Li, Z. Different phases of few-layer MoS_2 and their silver/gold nanocomposites for efficient hydrogen evolution reaction. *Catal. Sci. Technol.* **2020**, *10* (1), 154−163.
(31) Lee, S.; Kim, Y. K.; Hong, J.-Y.; Jang, J. Electro-response of MoS_2 Nanosheets-Based Smart Fluid with Tailorable Electrical Conductivity. *ACS Appl. Mater. Interfaces* **2016**, *8* (36), 24221−24229.
(32) Wang, X.; Tian, J.; Cheng, X.; Na, R.; Wang, D.; Shan, Z. Chitosan-Induced Synthesis of Hierarchical Flower Ridge-like MoS_2/N-Doped Carbon Composites with Enhanced Lithium Storage. *ACS Appl. Mater. Interfaces* **2018**, *10* (42), 35953−35962.
(33) Gong, C.; Long, M.; Xiao, J.; Li, J.; Chen, J.; Xiao, Y.; Zhang, G.; Gao, H.; Liu, H. One-Step Hydrothermal Reaction Induced Nitrogen-Doped MoS_2/MXene Composites with Superior Lithium-Ion Storage. *Batteries* **2022**, *8* (10), 156.
(34) Chen, J.; Xu, Z.; Hu, Y.; Yi, M. PEG-assisted solvothermal synthesis of MoS_2 nanosheets with enhanced tribological property. *Lubricat. Sci.* **2020**, *32* (6), 273−282.
(35) Shi, X.; Pan, L.; Chen, S.; Xiao, Y.; Liu, Q.; Yuan, L.; Sun, J.; Cai, L. Zn(II)-PEG 300 Globules as Soft Template for the Synthesis of Hexagonal ZnO Micronuts by the Hydrothermal Reaction Method. *Langmuir* **2009**, *25* (10), 5940−5948.
(36) Shao, J.; Qu, Q.; Wan, Z.; Gao, T.; Zuo, Z.; Zheng, H. From Dispersed Microspheres to Interconnected Nanospheres: Carbon-Sandwiched Monolayered MoS_2 as High-Performance Anode of Li-Ion Batteries. *ACS Appl. Mater. Interfaces* **2015**, *7* (41), 22927−22934.
(37) Koczkur, K. M.; Mourdikoudis, S.; Polavarapu, L.; Skrabalak, S. E. Polyvinylpyrrolidone (PVP) in nanoparticle synthesis. *Dalton Trans.* **2015**, *44* (41), 17883−17905.
(38) Safo, I. A.; Werheid, M.; Dosche, C.; Oezaslan, M. The role of polyvinylpyrrolidone (PVP) as a capping and structure-directing agent in the formation of Pt nanocubes. *Nanoscale Adv.* **2019**, *1* (8), 3095−3106.
(39) Kumari, S.; Gusain, R.; Kumar, N.; Khatri, O. P. PEG-mediated hydrothermal synthesis of hierarchical microspheres of MoS_2 nanosheets and their potential for lubrication application. *J. Ind. Eng. Chem.* **2016**, *42*, 87−94.
(40) Guo, S.; Zhang, Q.; Zhu, Z.; Xie, J.; Fan, J.; Xu, Q.; Shi, P.; Min, Y. Facile Synthesis of Molybdenum Disulfide Nanosheets/Nitrogen-Doped Porous Carbon Composites for High-Performance Anode Material in Lithium-Ion Batteries. *ChemistrySelect* **2017**, *2* (10), 3117−3128.
(41) Li, H.; Chen, Y.; Chen, H.; Zhang, M.; Bai, G.; Ding, Y. Strongly surface-bonded MoO_2 and N-doped hierarchical carbon nanoplates through interfacial Mo-NC bonds with superb room/low-temperature Li-storage performance. *J. Alloys Compd.* **2022**, *927*, 166968.
(42) Lin, J.; Shi, Y. H.; Li, Y. F.; Wu, X. L.; Zhang, J. P.; Xie, H. M.; Sun, H. Z. Confined MoS_2 growth in a unique composite matrix for ultra-stable and high-rate lithium/sodium-ion anodes. *Chem. Eng. J.* **2022**, *428*, 131103.
(43) Jiao, J.; Du, K.; Wang, Y.; Sun, P.; Zhao, H.; Tang, P.; Fan, Q.; Tian, H.; Li, Q.; Xu, Q. N plasma treatment on graphene oxide-MoS_2 composites for improved performance in lithium ion batteries. *Mater. Chem. Phys.* **2020**, *240*, 122169.

https://doi.org/10.1021/acsomega.3c10031
ACS Omega 2024, 9, 9792−9802